This is a preprint, the final version is subject to change, of the American Mineralogist (MSA)
Cite as Authors (Year) Title. American Mineralogist, in press.
(DOI will not work until issue is live.) DOI: http://dx.doi.org/10.2138/am-2017-5944

# (Revision 2) Raman Spectroscopy of Water-rich Stishovite and Dense High-Pressure Silica up to 55 GPa

Carole Nisr[1], Sang-Heon Shim[1], Kurt Leinenweber[2], Andrew Chizmeshya[2]

[1] *School of Earth and Space exploration, Arizona State University, Tempe, AZ 85287, United States*

[2]*Department of Chemistry and Biochemistry, Arizona State University, Tempe, AZ 85287, United States*

## Abstract

Recent studies have shown that mineral end-member phases (δ-AlOOH phase, phase H and stishovite) with rutile-type or modified rutile-type crystal structures and solid solutions between them in the $MgO$-$Al_2O_3$-$SiO_2$ system can store large amounts of water and can be stable at high pressures and high temperatures relevant to the Earth's lower mantle. The Al-H charge coupled substitution ($Si^{4+} \rightarrow Al^{3+} + H^+$) has been proposed to explain the storage capacity found in some of these phases. However, the amount of $H^+$ found in some recent examples does not match the expected value if such substitution is dominant, and it is difficult to explain the larger water storage in stishovite with such a mechanism alone. An octahedral version of the hydrogarnet-like substitution ($Si^{4+} \rightarrow 4H^+$) has been proposed to explain the incorporation of protons in Al-free, water-rich stishovite. Yet, the high-pressure structural behavior of OH in this phase has not yet been measured. In this study, we report high-pressure Raman spectroscopy measurements on Al-

free hydrous stishovite with 3.2±0.5 wt% water up to 55 GPa. At ambient pressure, we find that the OH stretching modes in this phase have frequencies lying in between those in low-water aluminous stishovite and those in δ-AlOOH, suggesting a strength of the hydrogen bonding intermediate between these two cases. After decompression to 1 bar, we observe modes that are similar to the IR-active modes of anhydrous and hydrous stishovite, suggesting that the existence of Si defects in the crystal structure can activate the inactive modes. For both lattice and OH-stretching modes, our data show a series of changes at pressures between 24 and 28 GPa suggesting a phase transition (likely to $CaCl_2$ type). While some of the lattice mode behaviors are similar to what was predicted for the AlOOH polymorphs, the OH mode of our hydrous stishovite shows a positive frequency shift with pressure, which is different from δ-AlOOH. All our spectral observations suggest that water-rich pure dense silica has a distinct proton incorporation mechanism from aluminous low-water stishovite and δ-AlOOH, supporting the proposed direct substitution.

# Introduction

A few nominally anhydrous minerals (NAMs) stable in the Earth's mantle, such as wadsleyite and ringwoodite, have been shown to store considerable amounts of $H_2O$ (up to a few wt%; e.g., Bell and Rossman, 1992; Smyth, 1994; Kohlstedt et al., 1996; Rossman, 1996; Hirschmann, 2006; Pearson et al., 2014). Such OH substitution in the the main mantle mineral phases opens up to the possibility that these phases could store a large amount of water in the Earth's deep interior. However, studies have indicated that the dominant minerals in the lower mantle, such as bridgmanite and ferropericlase, have a much lower storage capacity for water (less than 50 ppm) (Bolfan-Casanova et al., 2000, 2002, 2003; Panero et al., 2003, 2015), implying that the lower

mantle, which represents 55% of the Earth's volume, may be "dry" (Hirschmann, 2006; Karato 2011).

Although stishovite does not occur as a free phase in pyrolite under mantle-relevant conditions, it is believed to be one of the main mineral phases in the subducting oceanic crust (sediments and mid-oceanic ridge basalt, MORB) in the lower mantle, 10–20 vol% (Ono et al., 2001; Ricolleau et al., 2010; Grocholski et al., 2012). Stishovite can contain up to 4 wt% $Al_2O_3$ in Al-rich system, such as MORB (Irifune and Ringwood, 1993; Ono et al., 2001; Chung and Kagi, 2002; Liu et al., 2006; Bolfan-Casanova et al., 2009). Studies have shown that the dissolution of $Al_2O_3$ may enhance the water storage capacity of stishovite through a charge coupled substitution: $Si^{4+} \rightarrow Al^{3+} + H^+$. For example, Pawley et al. (1993) found that the $H_2O$ content of stishovite with more than 1 wt% $Al_2O_3$ is higher than that of pure stishovite by a factor of 10 (~100 ppm $H_2O$). Chung and Kagi (2002) and Litasov et al. (2007) have reported an even higher water content for Al-bearing stishovite: 844 ppm $H_2O$ for samples synthesized at 15 GPa and ~1700 K and 3010 ppm at 20 GPa and ~1700 K.

The stability of δ-AlOOH with a distorted rutile type structure in high pressure synthesis (Suzuki et al., 2000) suggests that an AlOOH component could account for the water storage in aluminous stishovite. However, the amount of H in aluminous stishovite samples is not nearly equal to the amount of Al. For example, Litasov et al. (2007) reported that only one seventh of Al incorporated into stishovite is associated with hydrogen. Bromiley et al. (2006) also reported excess Al in stishovite, not charge-balanced by hydrogen. Thus the incorporation of aluminum cannot be explained solely by the charge-coupled substitution with protons in stishovite. Other substitution mechanisms should also be present.

The recent discovery of the water-rich Mg-silicate phase, $(Mg,Si)O_2(OH)_2$ (phase H) (Tsuchiya, 2013; Nishi et al., 2014), and even a potential solid solution between this phase and δ-AlOOH (Ohtani et al., 2014), highlights the importance of understanding the water-storage mechanism in rutile type structures. The occurrence of this solid solution suggests that both phases may be more related to δ-AlOOH ($2Al^{3+} \rightarrow Mg^{2+} + Si^{4+}$), and therefore to a charge coupled substitution ($2Si^{4+} \rightarrow Mg^{2+} + Si^{4+} + 2H^{+}$). However, the stoichiometry, crystal structures, and OH environments of the hydrous phases are still not well known.

Spektor et al. (2011) found that at 10 GPa and 723 K as much as 1.3 wt% $H_2O$ (measured by TGA and SIMS) can be stored in stishovite without Al, resulting in an expansion of the unit cell. Spektor et al., (2016) obtained stishovite samples with TGA bulk water contents in excess of 3% at lower temperatures, which were interpreted as mixtures of a less hydrous and a more hydrous stishovite averaging to 3 weight percent $H_2O$. They attributed the significant $H_2O$ incorporation to a direct substitution of $4H^{+}$ for $Si^{4+}$ on the octahedral site. This finding reveals that under appropriate conditions, far more protons can be incorporated into stishovite through a substitution mechanism other than charge-coupling with Al.

Several models have been proposed for the OH-bonding in rutile-type phases and we compare three of them in Figure 1. Swope et al. (1995) reported 13,000 ppm $OH^{-}$ in natural rutile. The large amount is mainly due to trivalent cation substitution. Using neutron diffraction, they determined that the location of H is on the shared edge between the $TiO_6$ octahedra (Figure 1a). Spektor et al. (2011) proposed a different OH incorporation mechanism in their water-rich pure stishovite (Figure 1b). Their NMR data suggest that protons incorporate into the stishovite structure through a direct substitution of $4H^{+}$ for $Si^{4+}$ yielding octahedral hydrogarnet defects with the four protons clustered in hydroxyl groups around a silicon vacancy. Although hydrogen

88 atoms were not located directly, based on NMR and other evidence, they proposed a group of 4H
89 in a tetrahedral arrangement (Figure 1b). δ-AlOOH provides a third possible proton site in rutile-
90 type structures (Figure 1c). The hydrogen position was determined by Komatsu et al. (2006).
91 From *ab initio* calculations, Tsuchiya et al. (2002, 2008) have discussed different atomic
92 configurations for δ-AlOOH, with centered and off-centered hydrogen positions in the vacant
93 octahedral sites rather than the octahedra occupied by Si. The H in the off-centered configuration
94 resides between the nearest oxygen and contains an asymmetric O-H…O bond similar to that
95 directly observed by Komatsu et al. (2006), whereas the H in the centered configuration is on the
96 midpoint between the two nearest oxygens, with a symmetrized hydrogen bond.

97 It is possible that depending on the water content, different proton substitution mechanisms could
98 operate. In addition, different substitution mechanisms can exist together in one structure at a
99 given water content range. In fact, the chemical composition of the rutile type (or modified)
100 hydrous or water-rich phases in the mantle may be complicated, and the complex chemistry may
101 allow multiple substitution mechanisms in one structure. Therefore, it is of interest to understand
102 the dominant OH-bonding involved in water-rich Al-free stishovite and its high pressure
103 polymorphs, which can allow us to probe OH in the Al-free environment. In this study, we report
104 Raman spectra of water-rich Al-free stishovite and its high pressure polymorph over a range of
105 pressures.

# Experimental methods

We synthesized a hydrous stishovite sample from a mixture of $SiO_2$+$H_2O$ held at 9 GPa and 450°C for 49 hours in a 6/8 multi-anvil press using an 14/8 assembly (Leinenweber et al., 2012) at Arizona State University (ASU). Although our methods are similar to those of Spektor et al. (2011, 2016), we have made a few modifications with the goal of obtaining a single phase product with high water content. We used amorphous silica (1 micron grain size, SPEX, purity 99.999%) as a starting material to provide a metastable starting point and a short diffusion pathway for the hydration because of the slow kinetics at low temperatures. Spektor et al. (2016) has documented that a two-phases mixture of more hydrous and less hydrous stishovites are obtained in all cases with greater than 1.5 wt% $H_2O$. In order to produce a single-phase sample with higher $H_2O$ content, we used a smaller assembly (14/8 instead of 18/12) and prepared thick-walled silver, self-sealing capsules with a small sample chamber to reduce thermal gradients. Also, the run duration was extended from 8 to 49 hours. As in the previous study, $H_2O$ saturation was verified by checking for free $H_2O$ in the sample after the run was completed. Through these improvements in thermal homogeneity and reaction time, we were able to obtain a single phase (confirmed by X-ray diffraction and Raman) with an $H_2O$ content (determined from lattice parameters) of 3.2±0.5 wt%, which was not possible in Spektor et al. (2011, 2016) perhaps because of the larger sample chamber necessary to obtain an enough amount of the samples for TGA and NMR measurements.

126 The quality of the synthesized sample was examined using Raman spectroscopy and X-ray
127 diffraction. Diffraction measurements were performed at the GSECARS sector of the Advanced
128 Photon Source (Figure 2) and Raman spectroscopy was conducted at ASU (see below for detail).
129 Both Raman and XRD show that our sample has a single phase, stishovite. We found that the
130 diffraction pattern agrees qualitatively well with the expected diffraction pattern for anhydrous
131 stishovite (e.g., Andrault et al., 2003). However, the diffraction lines from our sample are
132 systematically shifted to lower diffraction angles, suggesting a larger unit-cell volume of our
133 hydrous stishovite sample than anhydrous stishovite. From the diffraction pattern, we obtained: $a$
134 = 4.2068 (9) Å, $c$ = 2.6669 (9) Å, and $V$ = 47.198 (21) Å$^3$. The $a$ axis and the unit-cell volume
135 are significantly different from the values reported for anhydrous stishovite by Andrault et al.
136 (2003): $a$ = 4.1776 (2) Å, $c$ = 2.6652 (3) Å, and $V$ = 46.513 (6) Å$^3$.

137 Because the incorporation of protons into $SiO_2$ stishovite causes a significant change in the unit
138 cell volume, the unit cell can be used to estimate the water content. Spektor et al. (2011) reported
139 the relationship between the water contents and the unit-cell volume in Al-free hydrous
140 stishovite samples. The maximum amount of water they found in a single-phase sample (1.3
141 wt%) is in the sample synthesized at 9 GPa and 450°C. Spektor et al. (2016) has published
142 additional data on hydrous stishovite samples with different water contents, including more
143 water-rich samples. Among the data reported in the paper, we use only the data points with all
144 necessary information (thermogravimetric analysis (TGA), unit-cell volumes, and weight
145 fractions) for constructing a calibration line for stishovite at 1 bar (Figure 3). The TGA traces
146 reported in Spektor et al. (2016) are for the samples from the 8-hour heating experiments with
147 $SiO_2$ glass + $H_2O$ as a starting material (Haussermann, pers. comm.). For the samples with two
148 stishovite phases (a more and less hydrous ones) in the paper, we obtained a unit-cell volume

149 value by averaging the two unit cell volumes with weights from phase fractions listed in Table 2
150 of Spektor et al. (2016). The minor weight loss from 25 °C to 400 °C before the onset of more
151 rapid weight loss was considered to be due to surface-adsorbed water, and was not included in
152 the final water content values for stishovite (Haussermann, pers. comm.). The line in Figure 3
153 can be used to estimate the water content of a hydrous stishovite sample from its measured unit-
154 cell volume.

155 Using this fitting, we obtained a water content of 3.2±0.5 wt% for our sample. This amount is
156 much higher than, for example, the pure stishovite sample synthesized at 15 GPa and 1200°C by
157 Bolfan-Casanova et al. (2000) (72 ppm), and Al-bearing stishovite synthesized by Pawley et al.
158 (1993) (82 ppm for 1.51 wt% Al), Chung and Kagi, (2002) (844 ppm for 1.26 wt% Al), Panero
159 et al. (2003) (400 ppm for 3 wt% Al), and Litasov et al. (2007) (2900 ppm for 4.6 wt% Al.

160 We cold-pressed the powder sample into a thin foil of about ~60×60 $\mu m^2$ in size and ~10 μm in
161 thickness. The sample was then loaded in a 140 μm diameter hole in a rhenium gasket indented
162 by diamond anvils with 200 μm culet diameter. The diamond anvils are ultra-low fluorescence
163 and are used to compress the sample in a symmetric-type diamond anvil cell (DAC). We loaded
164 a ruby chip next to the sample on the cylinder side that was used as a pressure calibrant. We
165 cryogenically loaded argon as a pressure transmitting medium using a dry Ar chamber of the
166 loading system at ASU.

167 We conducted Raman measurements at ASU. We used the 532 nm excitation line of a frequency
168 doubled Nd:YAG laser. From the reflectivity and absorption from the optical components in our
169 Raman system, the beam intensity should not exceed 30 mW at the surface of the sample. We
170 conducted measurements at spectral ranges of 44-830 $cm^{-1}$ and 462-1214 $cm^{-1}$ for the lattice

vibrations and 2724-3259 $cm^{-1}$ for the OH modes, using a 1800 grooves/mm grating. The spectrometer was calibrated using the neon emission spectra. In order to remove the pixel-to-pixel sensitivity differences in the CCD detector, we measured a spectrum of a glass with known fluorescence intensities at different wavenumbers. The measured spectra were fit to polynomial functions. The intensity correction function was applied for the measured Raman intensities before data analysis. Ruby fluorescence spectra were measured using the same spectroscopy system. We have conducted Raman measurements during compression up to ~55 GPa and during decompression to 0 GPa at room temperature. For each pressure during compression and decompression, data were collected for six minutes at the same spot on the sample. Raman spectra at 1 bar were collected before compression and after decompression.

# Raman spectra at 1 bar and 300 K

Infrared (IR) spectra on water-rich stishovite were measured by Spektor et al. (2011, 2016). However, Raman data have not yet been reported for the OH vibration even at 1 bar. We have measured both Raman-active lattice and OH vibrational modes in water-rich Al-free stishovite. The Raman-active OH modes of our pure stishovite with 3.2 wt% $H_2O$ (Figure 4) consist of 6 modes (Figure 4). These modes occur in a similar frequency range to some of the IR-active OH modes reported by Spektor et al. (2011) on pure stishovite with 1.3 wt% $H_2O$. Both contain bands in the region between 2800 and 3100 $cm^{-1}$. However, no Raman peaks were observed near the additional IR bands that were observed at lower frequencies of 2600–2700 and 3300–3400 $cm^{-1}$.

192 The OH stretching regions of water-rich stishovite in Raman (this study) and in IR (Spektor et
193 al., 2011, 2016) spectroscopy are very different from those reported in Al-bearing stishovite with
194 up to 3000 wt. ppm (0.3 wt.%) water (Pawley et al., 1993; Chung and Kagi, 2002; Panero et al.,
195 2003; Bromiley et al., 2006; Litasov et al., 2007; Thomas et al., 2009). The IR spectra from Al-
196 bearing stishovite with low water contents have an intense, broad and anisotropic band in the
197 region between 3000 and 3200 $cm^{-1}$ and various weak features around 3200–3300 $cm^{-1}$
198 (Bromiley et al., 2006, Litasov et al., 2007, Thomas et al., 2009) with a much weaker band at
199 2600–2700 $cm^{-1}$ in the diluted samples (Litasov et al., 2007). However, water-rich stishovite
200 shows strong IR and Raman bands at a lower frequency, at 2650–2900 and 2800–3100 $cm^{-1}$,
201 respectively. The stronger intensity at lower frequency indicates stronger hydrogen bonding in
202 water-rich stishovite. Bromiley et al. (2006) cautioned that even nominally Al-free samples
203 contain enough Al (8.2 ppm) to explain the water incorporation through the Al-H coupled
204 substitution. In our case, we used pure $SiO_2$, which may contain 10 or less ppm level of
205 impurities, such as Pt, B, and Al, estimated from our secondary ion mass spectrometry.
206 Furthermore, in our study and that of Spektor et al. (2011), the amount of water incorporated into
207 the crystal structure of stishovite is many orders of magnitude higher than that of Al, suggesting
208 that in our water-rich sample, the water incorporation should be fundamentally different from Al-
209 bearing stishovite; this conclusion is also supported by the differences identified in Raman and
210 IR active OH modes.

211 For water-rich stishovite, Spektor et al. (2011) proposed a hydrogarnet-like substitution (Figure
212 1b) with 4 OH groups on the octahedral Si defect. In this setup, two of the oxygens in the
213 octahedron are underbonded (therefore, they are possible acceptors of hydrogen bonds) and four
214 are possible OH sites. Spektor et al. (2011) focused on a possible geometry where the H atoms

215 are bonded to the four bridging oxygens, are directed in pairs towards the two remaining
216 oxygens, and are arranged in a tetrahedron because of the electrostatic repulsion (Figure 1b). In
217 its most symmetric arrangement, this configuration preserves a significant part of the symmetry
218 of the 2*a* Wyckoff site in stishovite, reducing the symmetry from point group *mmm* to 222. This
219 makes all four H sites equivalent by symmetry which would result in fewer Raman modes than if
220 the hydrogens went into a lower symmetry configuration. However, several other configurations
221 of OH on the octahedron can also be envisioned: more than one non-equivalent configurations on
222 different Si vacancies and/or thermal hopping between states on one vacancy). Therefore, the
223 high symmetry configuration in Figure 1b is not necessarily the only one that will be present in
224 nature.

225 All six of the Raman modes in the OH region are characteristic of moderate hydrogen bonding
226 with O–O distances ranging from 2.6 Å for the lowest frequencies to 2.7–2.75 Å for the highest
227 frequencies (e.g. Libowitzky and Rossman, 1997, Libowitzky. 1999). This is consistent with
228 hydrogen-bonding along the longer O–O distances in the octahedron. In anhydrous stishovite, the
229 shared edge is shortest (2.291 Å), the unshared apical edge is intermediate (2.522 Å), and the
230 along-chain unshared edge is longest (2.665 Å). The apical edge can be somewhat longer in
231 hydrous stishovite because of the expanded *a*-axis. Our Raman results are consistent with O–
232 H…O bonding along the apical edges of the octahedron, or the along-chain edges, or both, but
233 not likely along the shared edges because they are too short. Also, the inter-octahedral distance
234 in stishovite is 3.029 Å, which makes δ-AlOOH-type interoctahedral hydrogen-bonding unlikely.

235 A lone OH group would be associated with a single OH stretching mode, typically. It is not
236 currently known how many separate modes would be associated with the tetrahedral group of
237 hydrogens proposed for hydrous stishovite. Some dynamic coupling between the OH groups is

238 expected because of their proximity, through H-H repulsions and other interactions. Thus we
239 cannot tell for sure whether all five of the observed Raman modes come from one type of H
240 configuration, or whether several configurations are present in the sample at once.

241 The $AlO_6$ framework in the δ-phase of AlOOH is closely related to the $CaCl_2$ type structure
242 (Komatsu et al., 2006). Both are based on a departure from the rutile structure ($P4_2/mnm$) due to
243 rotations of the octahedra about the *c*-axis (in δ-AlOOH there is also a decentering due to the
244 effect of the hydrogens on the structure). In the case of δ-AlOOH, the rotations are extensive
245 enough that the oxygen sublattice closely approaches hexagonal-close packing (hcp) (cf.
246 O'Keeffe and Hyde, 1996). Because of the modifications to the structure, there should be
247 differences in vibrational spectra between those two phases and our water-rich stishovite.
248 Nevertheless, because the structures are related, vibrational spectra of δ-AlOOH should be able
249 to be compared to those of water-rich stishovite, particularly in the OH region. Raman studies of
250 δ-AlOOH have identified several broad OH stretching bands between 2000 and 2800 $cm^{-1}$ at 1
251 bar (Ohtani et al., 2001; Xue et al., 2006). Tsuchiya et al. (2008) have shown from first-
252 principles calculations that the calculated OH bands exist at similar wavenumber range as these
253 experimental bands. The OH stretching bands in δ-AlOOH occur at even lower frequencies than
254 those in our water-rich stishovite sample, indicating that the OH environment is different in both
255 structures; the OH is more strongly hydrogen-bonded in δ-AlOOH than in water-rich stishovite.

256 At 1 bar before compression (Figure 5, bottom), we have found four lattice modes that
257 correspond to the four fundamental Raman-active modes $B_{1g}$, $E_g$, $A_{1g}$, and $B_{2g}$ in anhydrous
258 stishovite (Table 1). At 1 bar after decompression, we have identified a total of 7 peaks in the
259 lattice mode frequency range between 180 and 1000 $cm^{-1}$ (Figure 5, top). We found that four of
260 the 7 modes are similar to the four active modes in anhydrous stishovite and the modes observed

before compression (Table 1). The frequencies of these four lattice modes are similar to that of anhydrous stishovite within ~2.5 $cm^{-1}$ (Hemley et al., 1986; Gillet et al., 1990; Kingma et al., 1995; McMillan et al., 1996). However, their full width at half maximum (FWHM) shows that they are considerably broadened in the spectrum of water-rich stishovite than in anhydrous stishovite by ~3 $cm^{-1}$ (Figure 5, bottom) and by ~9 $cm^{-1}$ when the sample is compressed to 55 GPa and then decompressed to 1 bar (Figure 5, top). Three of the 7 modes in the quench spectrum did not exist in water-rich stishovite before compression (Figure 5, bottom). They appeared at high pressure and survived after decompression (see discussion in the next section).

# High pressure Raman spectroscopy

With an increase in pressure, all the modes show frequency increases except for the mode at 235 $cm^{-1}$, which can be assigned to $B_{1g}$ based on its similarity to a mode at 232 $cm^{-1}$ in anhydrous stishovite at 1 bar (Kingma et al., 1995) (Figures 6a and 7a). At 5–10 GPa during compression, we found three new modes ($\nu_3$, $\nu_6$, and $\nu_9$). Two ($\nu_6$ and $\nu_9$) of the three modes remain in the spectra after decompression to 1 bar. We also found series of changes at pressures between 24 and 28 GPa, that include the appearance of new modes ($\nu_4$ and $\nu_5$), the splitting of two existing modes ($B_{1g}$ and $\nu_6$), the decrease in the rate of frequency shifts ($\nu_7$ and $\nu_{10}$), and the increase in the rate of frequency shift of the OH stretching mode (Figure 6d and 7b). As discussed below and also in our separate X-ray diffraction paper (Nisr et al., 2017, under revision), the changes at 24–28 GPa are associated with a transition to an orthorhombic phase, likely similar to the $CaCl_2$ type but with local differences due to the substituted Si sites.

With an increase in pressure up to 24 GPa, the stishovite $B_{1g}$ mode frequency decreases with a pressure slope of −1.07 $cm^{-1}$/GPa (Figures 6a and 7a). Similar softening has been reported for the related mode in anhydrous stishovite (Kingma et al., 1995) with a rate of −0.93 $cm^{-1}$/GPa at the same pressure range (Table 1). At the higher frequency side of $B_{1g}$, a broad feature ($\nu_2$) begins to develop at 23.1 GPa (Figure 6a). With further compression, this broad feature shows more defined peaks ($\nu_2$–$\nu_5$) (Figure 7a). They all show positive pressure shifts of frequency. Similar splitting was observed in anhydrous stishovite across the phase transition from the rutile type to the $CaCl_2$ type, but with a fewer peaks after the phase transition. In addition, $B_{1g}$ in anhydrous stishovite decreases more rapidly than in water-rich stishovite at the pressure close to the phase transition and shows stiffening after the transition. The softening of the $B_{1g}$ mode in stishovite followed by a stiffening of the $A_g$ mode in the $CaCl_2$ structure was also seen in hydrous Al-bearing stishovite at the phase transition at ~24 GPa (Lakshtanov et al., 2007b). However, we could not observe such a strong stiffening in water-rich stishovite. Also, we still observe a negative frequency shift of the $\nu_1$ mode in water-rich stishovite even after the phase transition (Figure 7a).

While the phase transition to $CaCl_2$-type in anhydrous stishovite is a second order transition (displacive) and occurs over a very small pressure interval, we found a significant pressure interval where both low- and high-pressure phases co-exist in water-rich stishovite in Raman (this study) and XRD (Nisr et al., 2017, under revision). Therefore, the continuing negative shift of the $\nu_1$ mode even after the phase transition could be the result of some stishovite remaining in the sample in the case of water-rich stishovite, due perhaps to a greater kinetic barrier for the phase transition in this system at 300 K than in anhydrous stishovite. In fact, the intensity of the $\nu_1$ mode decreases rapidly after the phase transition. Because the $B_{1g}$ mode shows a positive

frequency shift after the phase transition in anhydrous stishovite (Kingma et al., 1995), we can assign $\nu_2$ to $A_g$ after the phase transition at 24–28 GPa. It is also possible that one of the broad $\nu_3$–$\nu_5$ modes are the broad band seen in the $CaCl_2$-type phase by Kingma et al. (1995). Kingma et al. (1995) attributed the similar feature to inhomogeneity in stress conditions. However, in our study the feature branches out to separate peaks, which are not consistent with the behavior expected for stress inhomogeneity and likely related to changes in the local structures. As discussed above, $\nu_1$ continues a negative shift at higher pressure. However, at ~40 GPa, the spectral features at the frequency range undergo reorganization, making it difficult to use them to determine the highest pressure stability of the rutile structure. In our XRD analysis (Nisr et al., 2017, under revision), we found that the low pressure phase remains up to ~42 GPa in water-rich dense silica.

In the Raman spectra of δ-AlOOH (Ohtani et al., 2001), four modes (Tables 1) exist at this low frequency range at 1 bar with the most intense mode existing at 277 $cm^{-1}$. Mashino et al. (2016) reported Raman modes of δ-AlOOH at high pressure. Below 5.6 GPa, they observed Raman modes at 320–430 $cm^{-1}$ and 620 $cm^{-1}$, which are similar to the modes reported for the $P2_1nm$ structure (asymmetric O-H bond) in the computational study by Tsuchiya et al. (2008). Above 5.6 GPa, those peaks disappeared and new peaks appeared at 450–540 $cm^{-1}$ and become more similar to the modes expected for the *Pnnm* structure (symmetric O-H bond) in Tsuchiya et al. (2008). The two new modes at 450 and 540 $cm^{-1}$ that appeared after the phase transition of δ-AlOOH seem to have similarities in their behavior with the $\nu_3$, $\nu_4$ and $\nu_5$ modes we identified in water-rich dense silica, respectively. Therefore, an alternative interpretation of the appearance of such broad feature can be a phase transition to the *Pnnm* structure proposed for δ-AlOOH.

At low pressures, the $E_g$ mode is already weak (Figure 6b). With further compression, it becomes even weaker and broader. Around 23 GPa, it starts to show an asymmetry and suddenly decreases in the rate of frequency shift. Unfortunately, because of the weakness of this mode, it is not clear whether a splitting exists similarly to anhydrous stishovite or it is just a change in the frequency slope. Stishovite $A_{1g}$ is an intense mode (Figure 6c) showing an increase in frequency and intensity with pressure. Its frequency is in good agreement with that in anhydrous stishovite (Kingma et al. 1995). It shows a small decrease in the rate of the frequency shift at 23.1 GPa and this change can be also found during decompression at 26.1 GPa (Figure 7a). This behavioral change at 23.1 GPa was not found in anhydrous stishovite (Kingma et al., 1995). The $B_{2g}$ mode is extremely weak and was observed only before and after the transition during compression, and at pressures less than 10 GPa during decompression (Figure 7a). Its positive frequency shift is also in agreement with that in anhydrous stishovite (Kingma et al., 1995).

During compression, new peaks appear near the frequency of $E_g$ at 5–10 GPa (Figure 6b): $\nu_6$ and $\nu_9$. They were not observed in Raman of anhydrous stishovite (Kingma et al., 1995) and are much broader than Raman-active modes of stishovite. These two modes show significantly low intensity after the phase transition at 24–28 GPa. While $\nu_9$ does not show any apparent changes at the pressure where other modes undergo changes, $\nu_6$ appears to split around 39 GPa. Both modes remain in the Raman spectrum after decompression to 1 bar (Figure 5). After decompression to 1 bar, we found that the frequencies of the $\nu_6$ and $\nu_9$ modes are similar to those of the IR-active modes ($E_u(1)$ and $E_u(2)$, Table 2) of anhydrous stishovite (Hofmeister et al., 1990) and water-rich stishovite (Spektor et al., 2011). Karki et al. (1997) have shown from high pressure ab initio calculations that the $E_u$ IR-active rutile type mode (with 579 $cm^{-1}$ at 1 bar) splits to $B_{2u}$ and $B_{3u}$ after the transition to the $CaCl_2$ type phase, which is similar to the behavior of $\nu_6$ in water-rich

dense silica that splits around 39 GPa. The appearance of those modes and their broadness could be due to the defect and disorder in hydrous silica structure that makes most phonon modes Raman active by breaking related symmetry. These two IR active modes are involved with an asymmetric motion of Si atoms at the center of the $SiO_6$ octahedra (Traylor et al. 1971). This symmetry-breaking at a Si site would occur if one of the neighboring Si atoms along the edge-sharing chain is replaced by four hydrogen atoms and the other is not, for example. We also recall that Spektor et al. (2011) reported two different Si sites from the NMR spectra of water-rich stishovite samples prepared similarly as our samples, which appears to be consistent with potential diversity in the short range structure near Si atoms in water-rich stishovite. Because these modes appear at lower pressure and weaken severely at 24−28 GPa, they are unlikely related to the phase transition at the pressure range. Instead, they might have existed from very low pressure (even at 1 bar) due to Si defects in water-rich stishovite. With an increase in pressure, the distortion in the structure might increase and produce much more noticeable intensity for detection.

The $\nu_3$ mode appears at pressures slightly lower than the phase transition pressure and higher than the appearance of IR-active modes. Therefore, it is unclear at the moment whether the feature is indicative of Si defect or phase transition in dense water-rich silica. According to Karki et al. (1997), no IR-active mode exists at the frequency of the $\nu_3$ mode.

The frequencies of the lattice modes measured during decompression agree well with those measured during compression. With some degree of hysteresis, some new modes that appeared at the phase transition at 24–28 GPa (such as, $\nu_2$, $\nu_3$, $\nu_4$, and $\nu_5$), disappear with decompression. However, the strong mode at our lowest frequency ($\nu_1$) as well as $\nu_6$ and $\nu_9$ appear to survive until the decompression to 1 bar (Figure 5). The preservation of these modes after decompression

may indicate irreversible changes in the crystal structure of water-rich stishovite at 300 K by compression. However, all other modes disappear and the diffraction patterns remain the same after decompression (Nisr et al., 2017, under revision). Therefore, the change in the crystal structure may not be extensive and not all the structural aspect of the high pressure phase may remain at 1 bar after decompression.

For the OH region, we were able to identify all five modes separately up to 5.7 GPa. However, above the pressure, because it was difficult to resolve the detailed spectral features of OH modes, we fit the region to a broad single peak (Figure 6d). The evolution of this broad peak as a function of pressure is shown with circles on Figure 7b. Despite the data scatter, we found three regimes with different rate of increase in frequency, 5–23, 30–32, and 34–39 GPa using data points obtained during decompression. The pressure where the change was observed agrees with the pressure where we observed changes in lattice modes, particularly at 24–28 GPa for the phase transition. At the highest pressure regime, the OH mode becomes very weak.

We found a positive frequency shift in the OH mode as a function of pressure. The crystal structure of dense silica may become more distorted and the distance between neighboring O is increasing. This can explain the reason for the weakening of hydrogen bonding as the distortion progresses, as indicated by the increase in average OH frequency. In particular, the likely short distances between four hydrogen atoms in this structure, leading to likely H-H repulsions, and the fact that there is only one acceptor oxygen for every two hydrogens, represents a special case and this may explain the O-H frequency increase with pressure.

Tsuchiya et al. (2008) have showed from first principle calculations that δ-AlOOH modes frequencies decrease under pressure leading to hydrogen bond symmetrization and gradually increase after the symmetrization. The hydroxyl of asymmetric hydrogen bonds has a higher

396 stretching frequency. The increase of the OH modes frequencies in water-rich stishovite with
397 pressure and the similarity of two of the new modes $\nu_3$, $\nu_4$ and $\nu_5$ indicate that the bond
398 symmetrization does not occur in hydrous silica under pressure and the OH bonding in water-
399 rich stishovite is fundamentally different from that in δ-AlOOH, consistent with the different
400 substitution mechanism for H in the crystal structure.

401

# 402 Insights on the proton substitution in water-rich stishovite

403 Our Raman spectra are consistent with localized defects, in which each Si defect contains 4
404 hydrogens that are mainly bonded within that defect as proposed in Spektor et al. (2011). After
405 the rutile type to the $CaCl_2$ type transition, octahedral rotation occurs, but extreme rotation such
406 as that observed in δ-AlOOH is not yet observed even at the highest pressures reached in this
407 study. Our lattice parameter data (Nisr et al., 2017, under revisions) indicate that the octahedral
408 rotation is about halfway to the *hcp* limit of 9.74° (O'Keeffe and Hyde, 1996). Previous studies
409 have shown that the typical δ-AlOOH bonding is associated with a strong hydrogen bond
410 between the octahedral chains, rather than within the octahedra. This is characterized by already
411 very low OH stretching frequencies at ambient pressure, that decrease further with pressure,
412 which occurs because of the short inter-octahedral O-O distance caused by the extensive
413 octahedral rotation, and the fact that Al occupies all of the octahedra in the structure leading to
414 an underbonding of all the O sites by half of a charge unit. The fact that both the donor and
415 acceptor oxygens are equally underbonded, may also enhance the tendency toward symmetrical
416 hydrogen-bonding.

In contrast, in water-rich stishovite, we observe higher OH stretching frequencies that generally increase with pressure, indicative of weaker hydrogen bonding. We interpret the Raman data more consistent with the structural model by Spektor et al. (2011) where the $H_4O_6$ octahedra are present. The $H_4O_6$ octahedra are likely isolated from each other because of low enough concentration. In this case, the bonding between the second-neighbor octahedra similar to that in δ-AlOOH would not occur. Instead, in a $H_4O_6$ octahedron, each hydrogen tends to associate with one oxygen that has a bond valence deficit of ⅔ (thick solid gray lines in Figure 1 b) while the two remaining oxygens each act as acceptors for two hydrogen bonds at once (thick dashed gray lines in Figure 1b). The four hydrogens are also in close enough proximity for significant H-H repulsion. Therefore, with compression of the $H_4O_6$ octahedra, the O-H bonds may rotate away from the center of the octahedra to avoid the repulsion but also away from accepter oxygens as shown in Figure 1b by the black arrows. This overall bonding situation may result in a frequency increase with pressure observed in our Raman study. Yet, it is also important that the H configuration should be examined directly through neutron diffraction or other experiments.

The OH substitution could be much more complicated in the rutile type hydrous phases in the mantle because of their complex chemistry. Therefore, the bonding sites proposed by Swope et al. (1995) (Figure 1a) are possible, but so are many others and the four H on the defect have to be considered in combination rather than separately. Also, the total concentration of silica defects will be an important factor to consider: for example, for isolated defects (low concentrations of H), hydrogen bonding within the defect should predominate, while if defects are more abundant, hydrogen bonding between defects could also begin to occur, resembling that in δ-AlOOH. The likelihood of δ-AlOOH-type hydrogen bonding also increases when the $CaCl_2$-type distortion is

present because that distortion can bring neighboring defects closer together as the oxygen packing perpendicular to the *b*-axis approaches *hcp*.

# Implications for the phase transition in stishovite

Previous studies have shown that anhydrous Al-free stishovite undergoes a displacive second-order phase transition to the orthorhombic $CaCl_2$ structure (*Pnnm*) at ~50 GPa (Tsuchida et al., 1989; Kingma et al., 1995; Andrault et al., 1998; Hemley et al., 2000; Ono et al., 2002a; Andrault et al., 2003). Bolfan-Casanova et al. (2009) reported that anhydrous Al-bearing stishovite (with an average Al content of 2.9 wt% $Al_2O_3$) undergoes a phase transition to the $CaCl_2$-type structure at ~23 GPa. However, Ono et al. (2002b) did not observe any phase transition in Al-bearing stishovite up to 40 GPa. Although the end-member transition is believed to be nearly second-order based on reversals in the diamond-anvil cell (Kingma et al., 1995), the transition could become first-order in the presence of OH in silica (Umemoto et al., 2016). There is some indication of this in the Al-bearing cases because pressure hysteresis is observed in the rutile to $CaCl_2$ transition in these solid solutions (e.g. Bolfan-Casanova et al., 2009). This first-order character appears to be even stronger in the current case of $H_2O$-rich stishovite.

As known, stishovite can contain some additional water in conjunction with the Al incorporation (Pawley et al., 1993; Chung and Yagi, 2002; Litasov et al., 2007), or without Al (Pawley et al., 1993, Bolfan-Casanova et al., 2000; Bromiley et al., 2006; Litasov et al., 2007; Spektor et al., 2011). The amount of hydrogen is not close to the quantity needed for the charge balance, indicating that oxygen vacancies are still an important charge-balance mechanism for the

aluminum substitution in stishovite under these conditions. Interestingly, the incorporation of Al and H in stishovite significantly lowers the transition pressure to the $CaCl_2$ type polymorph (Lakshtanov et al., 2005; 2007).

Depending on $Al_2O_3$ and $H_2O$ contents in silica phases, the pressure of the post-stishovite phase transition may be variable and occur over a wide depth range in the lower mantle. Hydrogen bonds and/or the effect of the presence of the Al octahedra could play an important role in changing the transition pressure. This effect was observed by Lakshtanov et al. (2007) who found that the incorporation of Al and some water into silica reduces significantly the post-stishovite transition pressure in $SiO_2$ to 20–24 GPa and 300 K, with 6.1 wt% $Al_2O_3$ and 0.24 wt% $H_2O$.

In our case, the transition pressure to the $CaCl_2$ type phase occurs around 24 GPa in Al-free hydrous stishovite with 3.2 wt% water. The presence of aluminum and/or hydrogen therefore decreases the pressure of the phase transition to $CaCl_2$-type by ~30 GPa in comparison to anhydrous Al-free stishovite. However, the amount of Si defect, of Al, of H, the level of oxygen vacancies, and the different possible types of the H sites present in the stishovite can all play a role on how much the transition pressure decreases.

# Acknowledgement

We thank Ulrich Haussermann for providing TGA traces and valuable discussions on the water contents of hydrous stishovite samples. We thank the two anonymous reviewers and the associate editor for the discussion which greatly improved this paper. This work was supported

481 by an NSF grant to KL, SHS, and CN (EAR1321976). The results reported herein also
482 benefitted from collaborations and/or information exchange within NASA's Nexus for Exoplanet
483 System Science (NExSS) research coordination network sponsored by NASA's Science Mission
484 Directorate.

485

# References

Andrault, D., Fiquet, G., Guyot, F., and Hanfland, M. (1998) Pressure-induced Landau-type transition in stishovite. Science, 282, 720-724.

Andrault, D., Angel, R.J., Mosenfelder, J.L., and Le Bihan, T. (2003) Equation of state of stishovite to lower mantle pressures. American Mineralogist, 88, 301-307.

Bell, D. R., and Rossman, G. R. (1992) Water in Earth's mantle: the role of nominally anhydrous minerals. Science, 255, 1391.

Bolfan-Casanova, N., Keppler, N.H., and Rubie, D.C. (2000) Water partitioning between nominally anhydrous minerals in the $MgO–SiO_2–H_2O$ system up to 24 GPa: implications for the distribution of water in the Earth's mantle. Earth and Planetary Science Letters, 182, 209-221.

Bolfan-Casanova, N., Mackwell, S., Keppler, H., McCammon, C., and Rubie, D.C. (2002) Pressure dependence of H solubility in magnesiowüstite up to 25 GPa: Implications for the storage of water in the Earth's lower mantle. Geophysical Research Letters, 29, 89-1-89-4.

Bolfan-Casanova, N., Keppler, H., and Rubie, D.C. (2003) Water partitioning at 660 km depth and evidence for very low water solubility in magnesium silicate perovskite. Geophysical Research Letters, 30.

Bolfan-Casanova, N., Andrault, D., Amiguet, E., and Gignot, N. (2009) Equation of state and post-stishovite transformation of Al-bearing silica up to 100 GPa and 3000K. Physics of the Earth and Planetary Interiors, 174, 70-77.

505 Bromiley, G.D, Bromiley, F.A., and Bromiley, D.W. (2006) On the mechanisms for H and Al
506 incorporation in stishovite. Physics and chemistry of minerals, 33, 613-621.

507 Chung, J.I., and Kagi, H. (2002) High concentration of water in stishovite in the MORB system.
508 Geophysical research letters, 29, 16-1-16-4.

509 Gillet, P., Le Cléac'h, and M.M. (1990) High-temperature Raman spectroscopy of $SiO_2$ and
510 $GeO_2$ Polymorphs: Anharmonicity and thermodynamic properties at high-temperatures. Journal
511 of Geophysical Research: Solid Earth, 95, 21635-21655.

512 Grocholski, B., Catalli, K., Shim, S.-H., and Prakapenka, V. (2012) Mineralogical effects on the
513 detectability of the postperovskite boundary. Proceedings of the National Academy of Sciences,
514 109, 2275-2279.

515 Hemley, R.J., Mao, H.-K., and Chao, E.C.T. (1986) Raman spectrum of natural and synthetic
516 stishovite. Physics and chemistry of Minerals 13, 285-290.

517 Hemley, R.J., Shu, J., Carpenter, M.A., Hu, J., Mao, H.-K., and Kingma, K.J. (2000) Strain/order
518 parameter coupling in the ferroelastic transition in dense $SiO_2$. Solid State Communications, 114,
519 527-532.

520 Hirschmann, M.M. (2006) Water, melting, and the deep Earth $H_2O$ cycle. Annuual Review of
521 Earth and Planetary Sciences, 34, 629-653.

522 Hofmeister, A.M., Xu, J., and Akimoto, S. (1990) Infrared spectroscopy of synthetic and natural
523 stishovite. American mineralogist, 75, 951-955.

524 Irifune, T., and Ringwood, A.E. (1993) Phase transformations in subducted oceanic crust and
525 buoyancy relationships at depths of 600–800 km in the mantle. Earth and Planetary Science
526 Letters, 117, 101-110.

527 Jiang, F., Gwanmesia, G.D., Dyuzheva, T.I., and Duffy, T.S. Elasticity of stishovite and acoustic
528 mode softening under high pressure by Brillouin scattering. Physics of the Earth and Planetary
529 Interiors, 172, 235-240.

530 Kagi, H., Ushijima, D., Sano-Furakawa, A., Komatsu, K., Iizuka, R., Nagai, T., and Nakano, S.
531 (2010) Infrared absorption spectra of δ-AlOOH and its deuteride at high pressure and implication
532 to pressure response of the hydrogen bonds. Journal of Physics: Conference Series, 012052.

533 Karato, S.-I. (2011) Water distribution across the mantle transition zone and its implications for
534 global material circulation. Earth and Planetary Science Letters, 301, 413-423.

535 Karki, B.B., Warren, M.C., Stixrude, L., Ackland, G.J., and Crain, J. (1997) Ab initio studies of
536 high-pressure structural transformations in silica. Physical Review B, 55, 3465.

537 Kingma, K.J., Cohen, R.E., Hemley, R.J., and Mao, H.K. (1995) Transformation of stishovite to
538 a denser phase at lower-mantle pressures. Nature, 374, 243-245.

539 Kohlstedt, D.L., Keppler, H., and Rubie, D.C. (1996) Solubility of water in the α, β and γ phases
540 of $(Mg,Fe)_2SiO_4$. Contributions to Mineralogy and Petrology, 123, 345-357.

541 Komatsu, K., Kuribayashi, A.S., Ohtani, E., and Kudoh, Y. (2006) Redetermination of the high-
542 pressure modification of AlOOH from single-crystal synchrotron data. Acta Crystallographica
543 Section E: Structure Reports Online, 62, 216-218.

544 Lakshtanov, D.L., Vanpeteghem, C.B., Jackson, J.M., Bass, J.D., Shen, G., Prakapenka, V.,
545 Litasov, K., and Ohtani, E. (2005) The equation of state of Al, H-bearing $SiO_2$ stishovite to 58
546 GPa. Physics and chemistry of minerals, 32, 466-470.

547 Lakshtanov, D.L., Litasov, K.D., Sinogeikin, S.V., Hellwig, H., Li, J., Ohtani, E., and Bass, J.D.
548 (2007a) Effect of $Al^{3+}$ and $H^{+}$ on the elastic properties of stishovite. American Mineralogist, 92,
549 1026-1030.

550 Lakshtanov, D.L., Sinogeikin, S.V., Litasov, K.D., Prakapenka, V., Hellwig, H., Wang, J.,
551 Sances-Valle, C., Perillat, J.P., Chen, B., Somayazulu, M., and Li, J. (2007b) The post-stishovite
552 phase transition in hydrous alumina-bearing $SiO_2$ in the lower mantle of the earth. Proceedings
553 of the National Academy of Sciences, 104, 13588-13590.

554 Leinenweber, K.D., Tyburczy, J.A., Sharp, T.G., Soignard, E., Diedrich, T., Petuskey, W.B.,
555 Wang, Y., Mosenfelder, J. L. (2012) Cell assemblies for reproducible multi-anvil experiments
556 (the COMPRES assemblies). American Mineralogist, 97, 353-368.

557 Libowitzky, E., and Rossman, G. R. (1997) An IR absorption calibration for water in minerals.
558 American Mineralogist, 82, 1111-1115.

559 Libowitzky, E. (1999) Correlation of OH stretching frequencies and OH O hydrogen bond
560 lengths in minerals. Monatshefte fur Chemie, 130, 1047-1059.

561 Litasov, K.D., Ohtani, E., Kagi, H., Lakshtanov, D.L., and Bass, J.D. (2007) High hydrogen
562 solubility in Al-rich stishovite and water transport in the lower mantle. Earth and Planetary
563 Science Letters, 262, 620-634.

564 Liu, X., Nishiyama, N., Sanehira, T., Inoue, T., Higo, Y., and Sakamato, S. (2006)
565 Decomposition of kyanite and solubility of $Al_2O_3$ in stishovite at high pressure and high
566 temperature conditions. Physics and chemistry of minerals, 33, 711-721.

567 Mashino, I., Murakami, M., and Ohtani, E. (2016) Sound velocities of δ-AlOOH up to core-
568 mantle boundary pressures with implications for the seismic anomalies in deep mantle. Journal
569 of Geophysical Research: Solid Earth, 121, 595-609.

570 McMillan, P.F., Hemley, R.J., and Gillet, P. (1996) Vibrational spectroscopy of mantle minerals.
571 Mineral Spectroscopy: A Tribute to Roger G. Burns, Geochem. Soc. Spec. Publ 5 175-213.

572 Nishi, M., Irifune, T., Tsuchiya, J., Tange, Y., Nishihara, Y., Fujino, K., and Higo, Y. (2014)
573 Stability of hydrous silicate at high pressures and water transport to the deep lower mantle.
574 Nature Geoscience, 7, 224-227.

575 Ohtani, E., Litasov, K., Suzuki, A., and Kondo, T. (2001) Stability field of new hydrous phase,
576 δ-AlOOH, with implications for water transport into the deep mantle. Geophysical Research
577 Letters, 28, 3991-3993.

578 Ohtani, E., Amaike, Y., Kamada, S., Sakamaki, T., and Hirao, N. (2014) Stability of hydrous
579 phase H $MgSiO_4H_2$ under lower mantle conditions. Geophysical Research Letters 41, 8283-
580 8287.

581 O'Keeffe, M., and Hyde, B.G. (1996) Crystal Structures I. Patterns and Symmetry, 228 p.
582 Mineralogical Society of America, Washington, D.C.

583 Ono, S., Ito, E., and Katsura, T. (2001) Mineralogy of subducted basaltic crust (MORB) from 25
584 to 37 GPa, and chemical heterogeneity of the lower mantle. Earth and Planetary Science Letters,
585 190, 57-63.

586 Ono, S., Hirose, K., Murakami, M., and Isshiki, M. (2002a) Post-stishovite phase boundary in
587 $SiO_2$ determined by in situ X-ray observations. Earth and Planetary Science Letters, 197, 187-
588 192.

589 Ono, S., Suto, T., Hirose, K., Kuwayama, Y., Komabayashi, T., and Kikegawa, T. (2002b)
590 Letters. Equation of state of Al-bearing stishovite to 40 GPa at 300 K. American Mineralogist,
591 87, 1486-1489.

592 Panero, W.R., Benedetti, L.R., and Jeanloz, R. (2003) Transport of water into the lower mantle:
593 Role of stishovite. Journal of Geophysical Research: Solid Earth, 108, 2039.

594 Panero, W.R., Pigott, J.S., Reaman, D.M., Kabbes, J.E., and Liu, Z. (2015) Dry $(Mg,Fe)SiO_3$
595 perovskite in the Earth's lower mantle. Journal of Geophysical Research: Solid Earth, 120, 894-
596 908.

597 Pawley, A.R., McMillan, P.F., and Holloway, J.R. (1993) Hydrogen in stishovite, with
598 implications for mantle water content. SCIENCE-NEW YORK THEN WASHINGTON, 261,
599 1024 p.

600 Pearson, D.G., Brenker, F.E., Nestola, F., McNeill, J., Nasdala, L., Hutchison, M.T., Matveev,
601 S., Mather, K., Silversmit, G., Schmitz, S., and Vekemans, B. (2014) Hydrous mantle transition
602 zone indicated by ringwoodite included within diamond. Nature, 507, 221-224.

603 Ricolleau, A., Perillat, J.P., Fiquet, G., Daniel, I., Matas, J., Addad, A., Menguy, N., Cardon, H.,
604 Mezouar, M., and Guinot, N. (2010) Phase relations and equation of state of a natural MORB:
605 Implications for the density profile of subducted oceanic crust in the Earth's lower mantle.
606 Journal of Geophysical Research: Solid Earth, 115.B8.

607 Rossman, G.R. (1996) Studies of OH in nominally anhydrous minerals. Physics and Chemistry
608 of Minerals 23, 299-304.

609 Spektor, K., Nylen, J., Stoyanov, E., Navrotsky, A., Hervig, R.L., Leinenwever, K., Holland,
610 J.P., and Häussermann, U. (2011) Ultrahydrous stishovite from high-pressure hydrothermal
611 treatment of $SiO_2$. Proceedings of the National Academy of Sciences, 108, 20918-20922.

612 Spektor, K., Nylen, J., Mathew, R., Eden, M., Stoyanov, E., Navrotsky, A., Leinenweber, K.,
613 Häussermann, U. (2016). Formation of hydrous stishovite from coesite in high pressure
614 hydrothermal environments. American Mineralogist, 101, 2514-2524.

615 Smyth, J.R. (1994) A crystallographic model for hydrous wadsleyite β-$Mg_2SiO_4$): An ocean in
616 the Earth's interior? American Mineralogist, 79, 021-1024.

617 Suzuki, A., Ohtani, E., and Kamada, T. (2000) A new hydrous phase δ-AlOOH synthesized at 21
618 GPa and 1000 C. Physics and Chemistry of Minerals, 27, 689-693.

619 Swope, R.J., Smyth, J.R., and Larson. A.C. (1995) H in rutile-type compounds: I. Single-crystal
620 neutron and X-ray diffraction study of H in rutile. American Mineralogist, 80, 448-453.

621 Thomas, S.-M., Koch-Muller, M., Reichart, P., Rhede, D., Thomas, R., Wirth, R., and Matsyuk,
622 S. (2009) IR calibrations for water determination in olivine, r-$GeO_2$, and $SiO_2$ polymorphs.
623 Physics and Chemistry of Minerals, 36, 489-509.

624 Traylor, J.G., Smith, H.G., Nicklow, R.M., and Wilkinson, M.K. (1971) Lattice dynamics of
625 rutile. Physical Review B, 3, 3457.

626 Tsuchida, Y., and Yagi, T. (1989) A new, post-stishovite high pressure polymorph of silica.
627 Nature, 340, 217-220.

628 Tsuchiya, J., Tsuchiya, T., Tsuneyuki, S., and Yamanaka, T. (2002) First principles calculation
629 of a high-pressure hydrous phase, δ-AlOOH. Geophysical Research Letters, 29, 15-1-15-4.

630 Tsuchiya, T., Caracas, R., and Tsuchiya, J. (2004) First principles determination of the phase
631 boundaries of high-pressure polymorphs of silica. Geophysical research letters, 31, L11610.

632 Tsuchiya, J., Tsuchiya, T., and Wentzcovitch, R.M. (2008) Vibrational properties of δ-AlOOH
633 under pressure. American Mineralogist, 93, 477-482.

634 Tsuchiya, J. (2013) First principles prediction of a new high-pressure phase of dense hydrous
635 magnesium silicates in the lower mantle. Geophysical Research Letters, 40, 4570-4573.

636 Umemoto, K., Kawamura, K., Hirose, K., and Wentzcovitch, R.M. (2016) Post-stishovite
637 transition in hydrous aluminous $SiO_2$. Physics of the Earth and Planetary Interiors, 255, 18-26.

638 Xue, X., Kanzaki, M., Fukui, H., Ito, E., and Hashimoto, T. (2006) Cation order and hydrogen
639 bonding of high-pressure phases in the $Al_2O_3$-$SiO_2$-$H_2O$ system: An NMR and Raman study.
640 American Mineralogist, 91, 850-861.

641

# Figure captions

Figure 1: Proposed OH configurations (black spheres with gray sticks) in the crystal structures of (a) low-water stishovite (Swope et al., 1995), (b) water-rich stishovite (Spektor et al., 2011), and (c) δ-AlOOH (Tsuchiya et al., 2002). The octahedra represent the $SiO_6$ (a and b) and $AlO_6$ (c) units in the crystal structures. In (b), the gray dashed line indicate hydrogen bonding and the black arrows indicate possible rotation of the O-H bonds with compression.

Figure 2: X-ray diffraction pattern of hydrous stishovite at 1 bar and 300 K. The pattern was collected at the GSECARS sector of the Advanced Photon Source using a monochromatic X-ray beam with a wavelength of 0.3344 Å and a beamsize of 3×4 $\mu m^2$. Numbers attached to peaks are Miller indices and the dotted lines show the offset in peak positions between anhydrous and hydrous stishovite of this study (lattice parameters of anhydrous stishovite in this study are: $a$ = 4.1805 (9) Å, $c$ = 2.6671 (9) Å, and $V$ = 46.612 (21) $Å^3$). The background of the pattern was subtracted.

Figure 3: Relationship between the unit-cell volumes of the hydrous stishovite samples and their water contents at 1 bar from the x-ray and TGA data of Spector et al. (2016) (black circles). The plot presents a lower bound based on the weight loss in TGA above 400-500 $^oC$. The water content ($w$) can be estimated directly from the measured unit cell volume ($V_{unit\text{-}cell}$) using the relation of $w$ (wt%) = 4.64±0.57 ($V_{unit\text{-}cell}$ ($Å^3$) – 46.515) in the range of 0-4 wt% water. The light grey area represents estimated 1σ uncertainties. From the relation, we obtained 3.2±0.5 wt% for our sample.

Figure 4: Raman spectra of hydrous stishovite at the OH stretching region at 1 bar and 300 K (a) before compression and (b) after decompression. The dashed lines are the fits of the spectrum after decompression.

Figure 5: Raman spectra of hydrous stishovite at 1 bar and 300 K before compression (bottom), and after decompression (top). $\nu_1$, $\nu_6$ and $\nu_9$ (cf. Figure 5) represent extra peaks that are not seen in anhydrous stishovite (Hemley et al., 1986; Gillet et al., 1990; Kingma et al., 1995; Jiang et al., 2009) nor in hydrous Al-bearing stishovite (Lakshtanov et al., 2007a), and that appeared after the sample was compressed to 41 GPa and the decompressed to 1 bar. The backgrounds of the spectra were subtracted. Stars represent noise that does not correspond to any Raman peak of the sample.

Figure 6: Raman spectra of the hydrous silica sample at 300 K at different pressures during compression. Red lines represent unknown Raman peaks that have never been seen before in Raman spectroscopy of anhydrous stishovite (Hemley et al., 1986; Gillet et al., 1990; Kingma et al., 1995; Jiang et al., 2009). (a,b,c) and d are hydrous silica lattice modes and OH mode, respectively. For clarity, spectra in (a,b) and c are ten and two times offset, respectively. The dashed lines are guide to eye showing the evolution of each mode with pressure.

Figure 7: (a) Pressure dependence of the Raman mode frequencies of water-rich dense silica up to 41 GPa during compression (closed circles) and decompression (open circles). Black circles are the modes known in anhydrous stishovite and red circles are new modes which were not documented in anhydrous stishovite and anhydrous $CaCl_2$ type phase. The crosses represent the frequencies of anhydrous stishovite reported in Kingma et al. (1995). The dashed and solid lines are guide to the eye indicating an approximate trend of the data. (b) Pressure dependence of the Raman frequencies of OH up to 41 GPa. At 0, 1.8 and 5.7 GPa, more features were identified in

685 the OH region above 5.7 GPa, they are fitted as a single broad band. The grey in (A) and (B)
686 indicates the approximate pressure range where the rutile type to $CaCl_2$ type phase transition
687 occurs in water-rich pure dense silica.

688

# Tables

Table 1: Mode frequencies ($\nu_i$) at 1 bar and isothermal pressure shifts ($d\nu_i/dP$) of the Raman active modes of water-rich hydrous stishovite (hStv), anhydrous stishovite (ahStv) and hydrous aluminous stishovite (hAlStv), and frequencies of Raman active bands of δ-AlOOH. 1. This study; 2. Kingma et al. (1995); 3. Lakshtanov et al. (2007a); 4. Lakshtanov et al. (2007b); 5. Ohtani et al. (2001). $\nu_1$, $\nu_6$ and $\nu_9$ are extra peaks seen in the Raman spectrum of hStv after the sample was compressed to 55 GPa and then decompressed to 1 bar.

| | | $B_{1g}$ | $E_g$ | $A_{1g}$ | $B_{2g}$ | $\nu_1$ | $\nu_6$ | $\nu_9$ |
|---|---|---|---|---|---|---|---|---|
| **hStv**[1] | $\nu_i$ ($cm^{-1}$) | 235 | 592 | 754 | 968 | 196 | 510 | 615 |
| | $d\nu_i/dP$ ($cm^{-1}$ $GPa^{-1}$) | -1.07 | 1.37 | 2.92 | 3.01 | | | |
| **ahStv**[2] | $\nu_i$ ($cm^{-1}$) | 232 | 589 | 754 | 966 | | | |
| | $d\nu_i/dP$ ($cm^{-1}$ $GPa^{-1}$) | -0.93 | 2.09 | 3.12 | 3.68 | | | |
| **hAlStv**[3,4] | $\nu_i$ ($cm^{-1}$) | 223 | 581 | 743 | 959 | | | |
| | $d\nu_i/dP$ ($cm^{-1}$ $GPa^{-1}$) | -0.49 | | | | | | |
| **δAlOOH**[5] | | **Mode 1** | **Modes 2** | **Modes 3** | **Modes 4** | | | |
| | $\nu_i$ ($cm^{-1}$) | 277 | 385/399/418 | 600/628 | 1203/1345/1389 | | | |

697 Table 2: Mode frequencies ($cm^{-1}$) at 1 bar of infrared absorption bands of water-rich hydrous stishovite
698 (hStv), anhydrous stishovite (ahStv) and δ-AlOOH. 1. Spektor et al. (2011); 2. Hofmeister et al. (1990); 3.
699 Kagi et al. (2010).

| | $E_u(1)$ | $E_u(2)$ | $E_u(3)$ | $A_{2u}$ |
|---|---|---|---|---|
| **hStv**[1] | 534 | 583 | 840 | |
| **ahStv**[2] | 520 | 620 | 800 | 950 |
| **δAlOOH**[3] | **Mode 1** | **Mode 2** | **Mode 3** | **Mode 4** |
| | 850 | 990 | 1180 | 1330 |

700

This is a preprint, the final version is subject to change, of the American Mineralogist (MSA)
Cite as Authors (Year) Title. American Mineralogist, in press.
(DOI will not work until issue is live.) DOI: http://dx.doi.org/10.2138/am-2017-5944

701 Figure 1

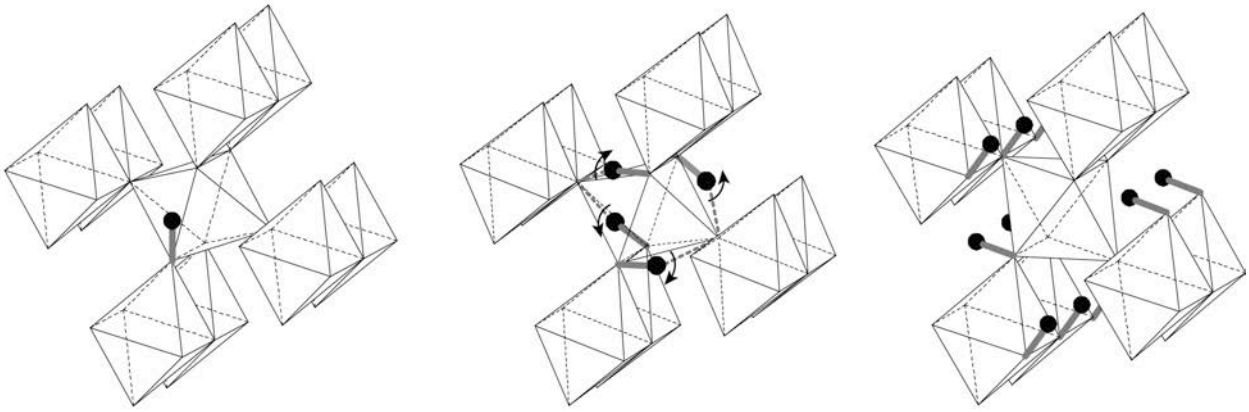


702

703

704 Figure 2

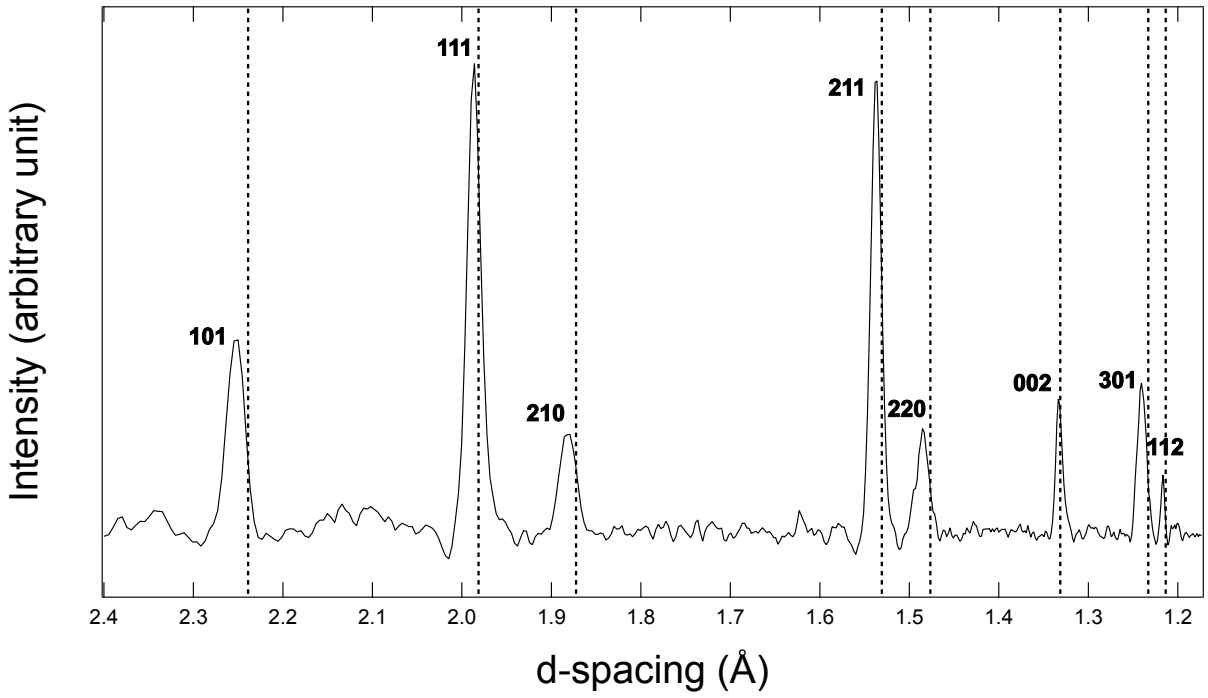


705

This is a preprint, the final version is subject to change, of the American Mineralogist (MSA)
Cite as Authors (Year) Title. American Mineralogist, in press.
(DOI will not work until issue is live.) DOI: http://dx.doi.org/10.2138/am-2017-5944

706 Figure 3

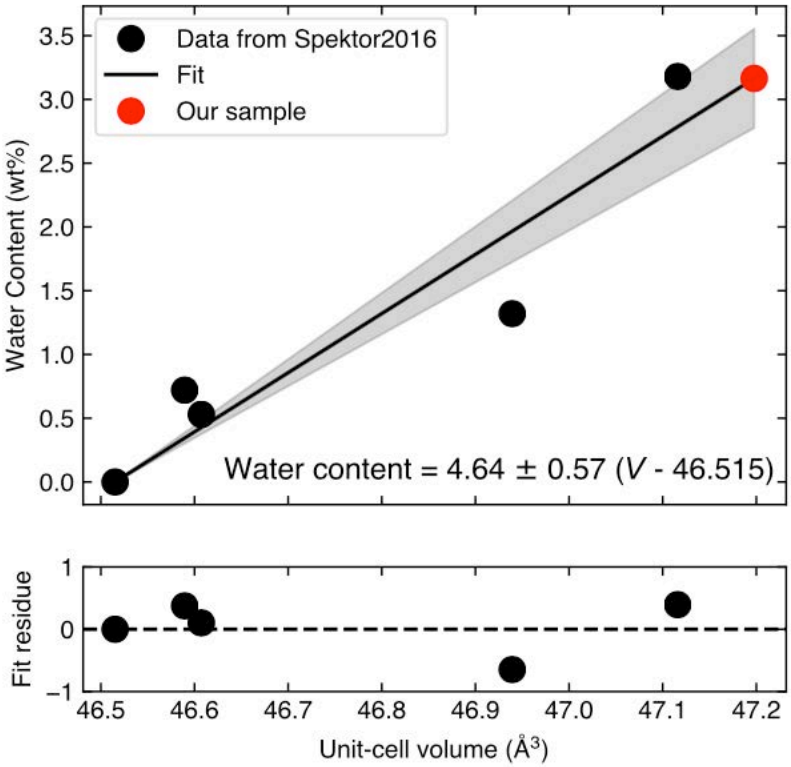


707

This is a preprint, the final version is subject to change, of the American Mineralogist (MSA)
Cite as Authors (Year) Title. American Mineralogist, in press.
(DOI will not work until issue is live.) DOI: http://dx.doi.org/10.2138/am-2017-5944

708 Figure 4

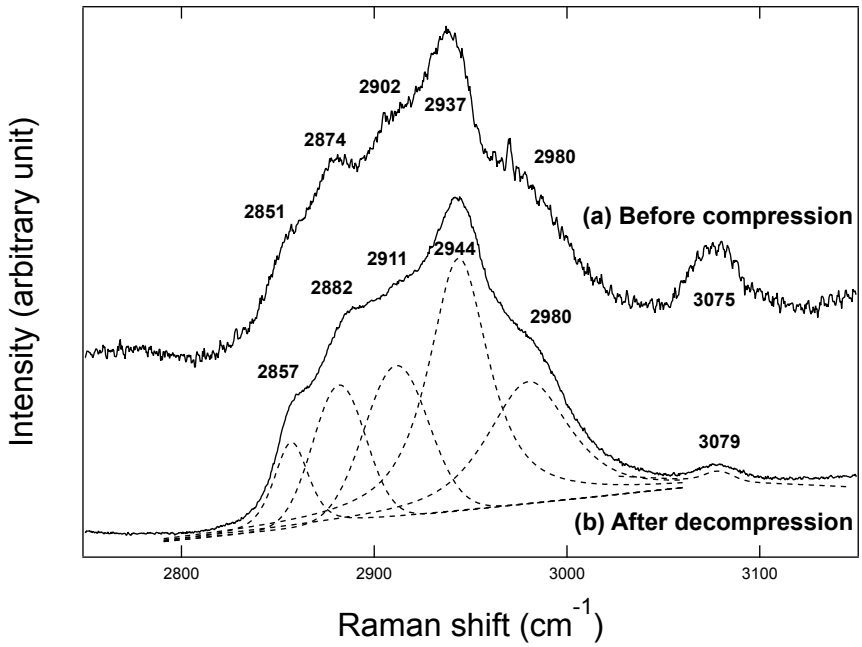


709

710 Figure 5

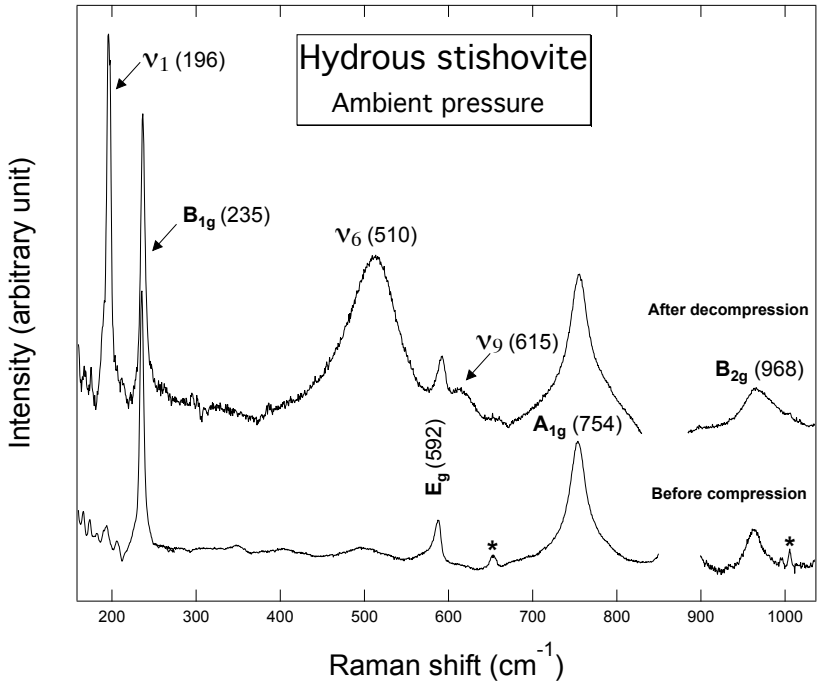


711

712

This is a preprint, the final version is subject to change, of the American Mineralogist (MSA)
Cite as Authors (Year) Title. American Mineralogist, in press.
(DOI will not work until issue is live.) DOI: http://dx.doi.org/10.2138/am-2017-5944

713 Figure 6

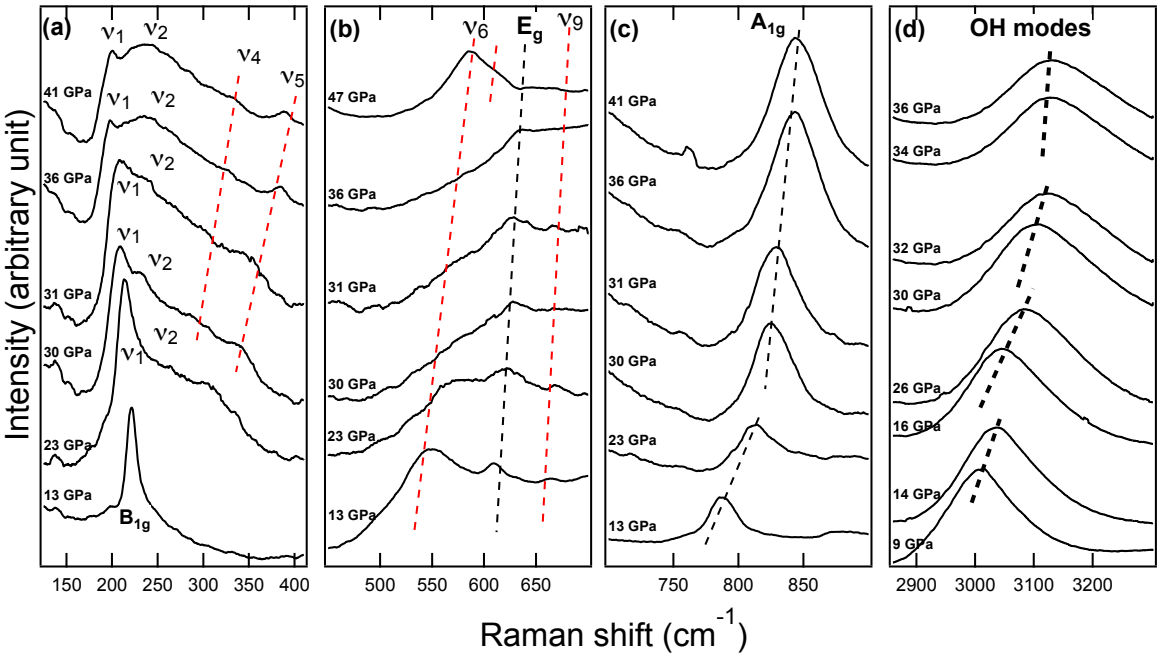


714

715 Figure 7

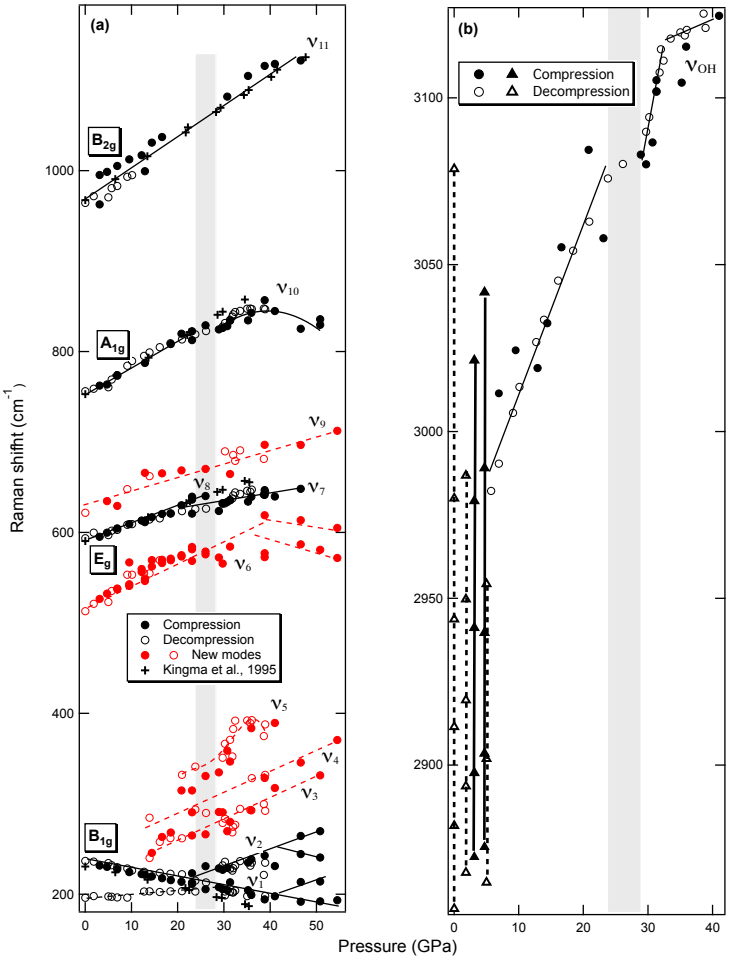


716